NONLINEAR NEURAL NETWORK MIXTURE MODELS FOR FRACTIONAL ABUNDANCE ESTIMATION IN AVIRIS HYPERSPECTRAL IMAGES

Javier Plaza,[1] Pablo Martínez, Rosa Pérez, and Antonio Plaza

1. Introduction

The interpretation of mixed pixels is a key factor in the analysis of hyperspectral imagery. Mixed pixels are a mixture of more than one distinct substance, and exist for one of two reasons. Firstly, if the spatial resolution of the sensor is not high enough to separate different materials, these can jointly occupy a single pixel, and the resulting spectral measurement will be a composite of the individual spectra that reside within the pixel. Secondly, mixed pixels can also result when distinct materials are combined into a homogeneous mixture [1]. This circumstance occurs independent of the spatial resolution of the sensor.

A commonly used approach to mixed pixel classification has been linear spectral unmixing, which uses a linear mixture model (LMM) to estimate the abundance fractions of spectral signatures lying within a mixed pixel [2]. Although the LMM has been demonstrated in numerous applications to be a useful technique for interpreting remote sensing data with high dimensionality, the question of whether linear or non-linear processes dominate spectral signatures of mixed pixels is still an unresolved matter. It has been reported that the reflectance spectrum of a mixture is a systematic combination of the component reflectance spectra in the mixture (usually called endmembers in the literature). The combination tends to be linear if components of interest in a pixel appear in spatially segregated patterns. If, however, the components are in intimate association, light typically interacts with more than one component as it is multiply scattered, and the mixing systematics between the different components are highly nonlinear. Nonlinear effects are an area of active research in particular applications such as vegetation and canopy studies [3] or water quality assessment [4–5], where LMM generally result in poor mixture analysis accuracy.

Artificial neural networks (ANNs) have been widely studied in the literature as a promising alternative to accomplish the difficult task of estimating fractional abundances of endmember materials in hyperspectral scenes [6]. The advent of ANN approaches in hyperspectral analysis is mainly due to their power in pattern recognition and classification [7]. The problem of mixed pixels has been tackled before from an ANN-based perspective, specifically, associative ANNs have been used in the past to establish a linear mixture model based on endmembers. Despite these attempts, ANN-based nonlinear mixing techniques remain largely unexplored for general-purpose applications. Only the pioneering work by Guilfoyle and Chang [8], which constructed a neural architecture based on radial basis function (RBF) neural networks, can be considered as a general model for ANN-based nonlinear unmixing independent of specifical physical properties of the observed land-cover materials. Such specificity usually complicates nonlinear models in terms of both implementation and computational complexity, and prevents their generalization to different applications, which is one of the most powerful features of the LMM.

In this paper we describe a new methodology for inferring land cover fraction within hyperspectral scenes. The proposed methodology makes use of a modified multi-layer perceptron (MLP) neural network, whose entries are determined by a linear activation function provided by a Hopfield neural network (HNN). As a result, our combined HNN/MLP method uses the LMM to provide an initial abundance estimation in linear fashion, and then refines the linear estimation using a nonlinear mixing model. To the best of our knowledge, this is the first approach in the literature that integrates linear and

[1]Neural Networks & Signal Processing Group (GRNPS), Computer Science Dept. University of Extremadura, Spain
Contact e-mail: jplaza@unex.es, Phone: +34 927 257254, Fax: +34 927 257203

nonlinear unmixing concepts for fractional abundance estimation in hyperspectral imagery. The remainder of the paper is organized as follows. Section 2 describes an Automated Morphological Endmember Extraction algorithm that is used in this work to find adequate training samples for the proposed neural architecture. Section 3 describes the proposed HNN/MLP method. Section 4 conducts a series of experiments where simulated data, made up of real spectra collected by the NASA/JPL Airborne Visible and Infra-Red Imaging Spectrometer (AVIRIS), are used to investigate performance of our approach. The impact of noise, mixture complexity, and use of radiance/reflectance data on algorithm performance are investigated. Section 5 conducts experiments using nonlinearly mixed real data which consists of 13 data sets collected by a Relab spectrometer (a high resolution, bi-directional spectrometer at Brown University). Our results with simulated and real data indicate that the proposed methodology is useful, robust and efficient in the task of identifying land cover fractions from remotely sensed imagery at sub-pixel scales, in particular when nonlinear mixtures and/or low SNR conditions dominate the hyperspectral data. Section 6 summarizes our conclusions and provides hints at plausible future research.

2. Automated morphological endmember extraction

The algorithm used in this work to generate training samples for the proposed neural network architecture is the automated morphological endmember extraction (AMEE) algorithm [9]. It is the only available endmember extraction algorithm that makes simultaneous use of spatial and spectral information via multi-channel morphological processing [10]. The input to the AMEE method is the full image data cube, with no previous dimensionality reduction. Let $\boldsymbol{h}$ denote the input hyperspectral data cube and $\boldsymbol{h}(x, y)$ denote the pixel vector at spatial location (x, y). Similarly, let K be a kernel defined in the spatial domain of the image (the x - y plane). This kernel, usually called structuring element (SE) in mathematical morphology terminology, is translated over the image. The SE acts as a probe for extracting or suppressing specific structures of the image objects, according to the size and shape of the SE. Having the above definitions in mind, the AMEE method is based on the application of multi-channel erosion and dilation operations to the data. The above operations are respectively defined as follows.

$$(\boldsymbol{h} \otimes K)(x, y) = \arg\_\,\mathrm{Min}_{(s,t)\in K} \left\{ \sum_s \sum_t \mathrm{dist}\big(\boldsymbol{h}(x, y), \boldsymbol{h}(x+s, y+t)\big) \right\} \quad (1)$$

$$(\boldsymbol{h} \oplus K)(x, y) = \arg\_\,\mathrm{Max}_{(s,t)\in K} \left\{ \sum_s \sum_t \mathrm{dist}\big(\boldsymbol{h}(x, y), \boldsymbol{h}(x-s, y-t)\big) \right\} \quad (2)$$

where dist is the spectral angle mapper (SAM). Multi-channel erosion (respectively, dilation) selects the pixel vector which minimizes (respectively, maximizes) a cumulative distance-based cost function, based on the sum of the SAM distance scores between each pixel in the spatial neighborhood defined by K and all the other pixels in the neighborhood. As a result, multi-channel erosion extracts the pixel vector that is more similar to its neighbors as opposed to multi-channel dilation, which extracts the most spectrally distinct pixel in the neighborhood (endmember candidate). It should be noted that, according to the definition of morphological erosion and dilation, the above operations are sensitive to the size and shape of the SE used in the computation. In our application, a morphological eccentricity index (MEI) is defined for each endmember candidate by calculating the SAM distance between the pixel provided by the dilation operation and the pixel provided by the erosion. This operation is repeated for all the pixels in the scene, using SEs with a range of different sizes, until a final MEI image is generated. A set of endmembers signatures $\{\boldsymbol{e}_i\}_{i=1}^{N}$ is found by a fully automated approach which consists of two steps [9]: 1) automated segmentation of the MEI image and 2) Spatial/spectral region growing of resulting regions.

3. Proposed neural network architecture for solving the nonlinear mixing problem

Once a set of endmember signatures $\{\boldsymbol{e}_i\}_{i=1}^{N}$ has been extracted from the original image, our goal is to solve the mixing equation $\boldsymbol{h}(x,y)=\sum_{i=1}^{N} c_i \boldsymbol{e}_i$ for each hyperspectral image pixel $\boldsymbol{h}(x,y)$. Let us denote by $\boldsymbol{e}_i=[e_{1i}, e_{2i}, ..., e_{Li}]^T$ a pure endmember signature, where L is the number of spectral bands. Similarly, let $c_i = f(a_i)$ be the contribution of endmember signature $\boldsymbol{e}_i$ in the pixel given by a nonlinear mixing function f, where a_i is the real abundance fraction of $\boldsymbol{e}_i$ in the pixel. If we express the problem using a matrix notation, i.e. $\boldsymbol{E}=[\boldsymbol{e}_1, \boldsymbol{e}_2, ..., \boldsymbol{e}_N]$, $\boldsymbol{c}=[c_1, c_2, ..., c_N]$ and $\boldsymbol{a}=[a_1, a_2, ..., a_N]$, then our goal is to solve the equation $\boldsymbol{h}(x,y)=\boldsymbol{E}\boldsymbol{c}^T$ at each pixel. In this work, we propose to solve the linear part of the problem, i.e., $\boldsymbol{c}^T=\boldsymbol{E}^{-1}\boldsymbol{h}(x,y)$, by a modified Hopfield neural network (HNN). On other hand, the nonlinear part of the problem related with the mixing equation, i.e., $\boldsymbol{a}=f^{-1}(\boldsymbol{c})$, is solved by using a Multi-Layer Perceptron (MLP). The effectiveness of this approach has been demonstrated in previous work [4],[11].

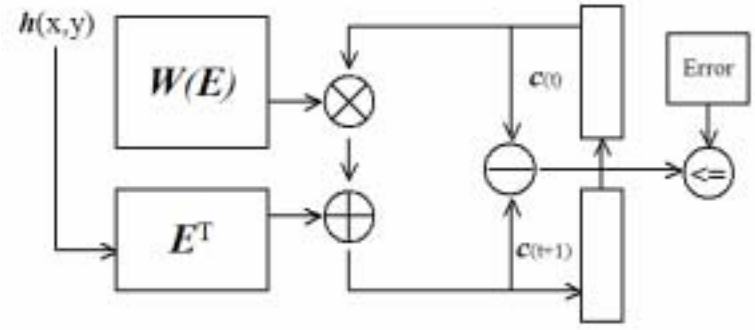

Figure 1. Schematic block diagram summarizing the performance of the HNN module.

3.1 Modified Hopfield neural network (HNN)

In order to solve the linear part of the mixing problem, we use a modified Hopfield neural network (HNN) with gradient descent learning based on error minimization (see Fig. 1). The number of input neurons is N, i.e., the dimension of the fractional abundance vector $\boldsymbol{c}$. A weight matrix W is created by using the sample correlation matrix between AMEE-derived endmember materials $\{\boldsymbol{e}_i\}_{i=1}^{N}$. The bias vector is dependent on the mixture spectrum under analysis. The proposed HNN is based on an iterative process where an initial abundance estimation $\boldsymbol{c}(t)$ is refined by multiplying $\boldsymbol{c}(t)$ by the weight matrix. The bias vector is then added and the result $\boldsymbol{c}(t+1)$ is compared to that obtained at the previous iteration until a desired threshold condition is satisfied for convergence.

3.2 Multi-layer perceptron (MLP)

In order to refine the HNN-based linearly derived contribution estimations obtained in the previous subsection, we propose to use a Multi-layer perceptron (MLP) neural network. The entries to the MLP are the outputs of the HNN, which we denote by $\boldsymbol{c}^i_{(HNN)}$, where $i=1, ..., N$. The number of input neurons is the same as the number of output neurons (see Fig. 2). The number of hidden neurons can be adjusted depending on the problem, and is only important in terms of convergence time. In this work, we have

used a recently developed concept of virtual dimensionality (VD), which estimates the number of distinct signal sources in the input data, to optimize the number of hidden neurons. On the other hand, the training process is based on error back-propagation criteria, where the output nodes and the hidden nodes modify their respective weight matrices (W and V in Fig. 2) depending on a pre-defined error (Delta), the input data, and an adjustable learning parameter Alpha (see Fig. 3). The delta error of the output layer is calculated as the difference between the abundance estimation ouputs $\boldsymbol{a}_i$, $i = 1, ..., N$ provided by the network architecture in Fig. 2 and a set of desired outputs given by ground truth fractional abundances available for the training samples. The resulting error is back-propagated to the hidden nodes until convergence is reached.

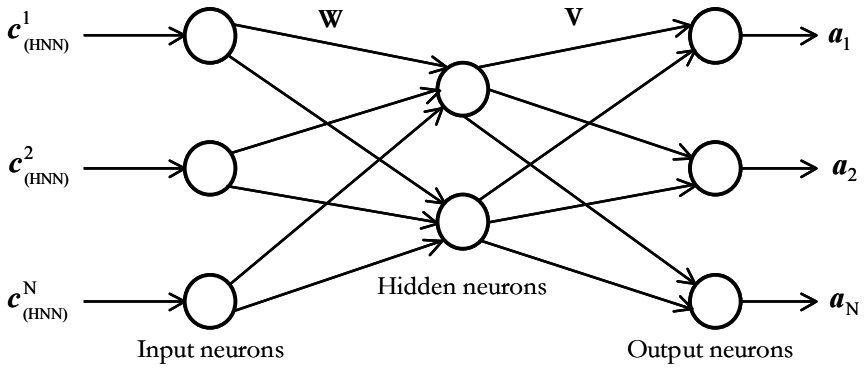

Figure 2. Architecture of the MLP module.

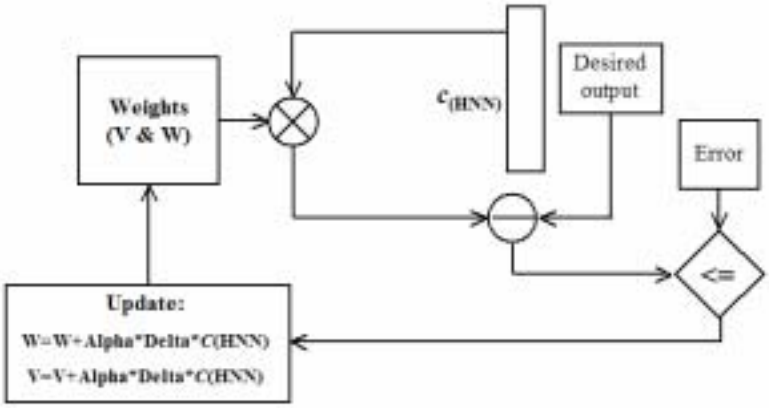

Figure 3. Schematic block diagram summarizing the performance of the MLP module.

4. Simulation experiments

One of the major problems involved in analyzing the quality of fractional abundance estimation methods in remotely sensed imagery is the fact that ground-truth information about the real abundances of materials at sub-pixel levels is very difficult (if not impossible) to obtain in real scenarios [10]. This fact has traditionally prevented the existence of comparative surveys using large databases of real images. In order to avoid this shortcoming, simulation of hyperspectral imagery has been suggested as a simple and intuitive way to perform a preliminary evaluation of analysis techniques [12]. The primary reason for the use of simulated imagery as a complement to real data analysis is that all details of the simulated images

are known. These details, such as noise, mixture complexity, and use of radiance/reflectance data, can be efficiently investigated because they can be manipulated individually and precisely. As a result, algorithm performance can be examined in a controlled manner.

In this section, we use simulated data based on real spectra collected by the AVIRIS imaging spectrometer [13] to accomplish the following experiments. Two AVIRIS imaging spectrometer datasets of the Jasper Ridge Biological Preserve (JRBP) in California have been selected for experiments. The datasets are available from http://aviris.jpl.nasa.gov. The datatets, acquired on April 1998, consist of 512x614 pixels and 224 spectral bands, with a nominal ground resolution of 20 m, spectral resolution of 10 nm, and 16-bit radiometric resolution. In a previous study of surface materials over JRBP, image endmembers were derived from the scenes above based on extensive ground knowledge. Fig. 4 plots spectral signatures associated with two of the main constituent materials at JRBP. These signatures, denoted as $\boldsymbol{r}_1$ (soil) and $\boldsymbol{r}_2$ (evergreen forest), will be used to construct two types of simulated data in this paper. Firstly, experiments with simulated linear mixtures are developed. These experiments will be mainly used to adjust input parameters such as Alpha and also to test the sensibility of the proposed HNN/MLP architecture against the signal-to-noise ratio (SNR). Secondly, nonlinear mixtures are simulated using a simple nonlinear function, the logarithmic function, to explore the accuracy of the proposed method in the presence of more complex mixtures. Simulation experiments will be used as a baseline to interpret results with real hyperspectral data, described in the following section. Next, we describe our simulation experiments.

4.1. Simulated linear mixtures

For this experiment, we have artificially mixed $\boldsymbol{r}_1$ and $\boldsymbol{r}_2$ in computer simulations to create a simulated scene containing linear mixtures. This scene, with a size of 100x100 pixels, is formed by 100 regions, $R_1,...,R_{100}$, of one-pixel width, representing linear mixtures between $\boldsymbol{r}_1$ and $\boldsymbol{r}_2$. Abundance fractions of $\boldsymbol{r}_1$ at region R_i are assigned by $(\mathrm{i}/100)$, while abundance fractions of $\boldsymbol{r}_2$ at $\boldsymbol{R}_\mathrm{i}$ are assigned by $1-(\mathrm{i}/100)$, as depicted in Fig. 5(a) and 5(b). The scene represents a subtle mixing scenario where $\boldsymbol{r}_1$ progressively infiltrates into $\boldsymbol{r}_2$ and vice versa. Random noise was added to the scene above to simulate contributions from ambient (clutter) and instrumental sources. White gaussian noise was created by using numbers with a standard normal distribution obtained from a pseudorandom number generator and added to each pixel. For the simulations, we consider the SNR for each band as the ratio of the 50% signal level to the standard deviation of the noise, hence following the definition given by Harsanyi and Chang [14]. This results in noise standard deviation that is roughly proportional to the average signal, a phenomenon often observed in radiometric data. Thus, the simulated hyperspectral data were created, based on a simple linear mixture model, by the following expression:

$$\boldsymbol{s}(\mathrm{x},\mathrm{y}) = \left(\frac{\mathrm{SNR}}{2} + \boldsymbol{n}(\mathrm{x},\mathrm{y})\right) \cdot \left(\sum_{\mathrm{j}=1}^{2} \boldsymbol{r}_\mathrm{j} \cdot \alpha_\mathrm{j}(\mathrm{x},\mathrm{y})\right) \tag{3}$$

where $\boldsymbol{s}$ denotes a vector containing the simulated discrete spectrum at the pixel with spatial coordinates (x,y) of the simulated image, $\alpha_\mathrm{j}(\mathrm{x},\mathrm{y})$ is the assigned fractional abundance of spectral signature at the pixel (x,y), and $\boldsymbol{n}(\mathrm{x},\mathrm{y})$ is the noise factor. Abundance sum-to-one and non-negativity constraints have been imposed in the expression in order to provide the simulation with adequate physical meaning. Six different SNR values, i.e., 10:1, 30:1, 50:1, 70:1, 90:1 and 110:1, were considered in the simulations.

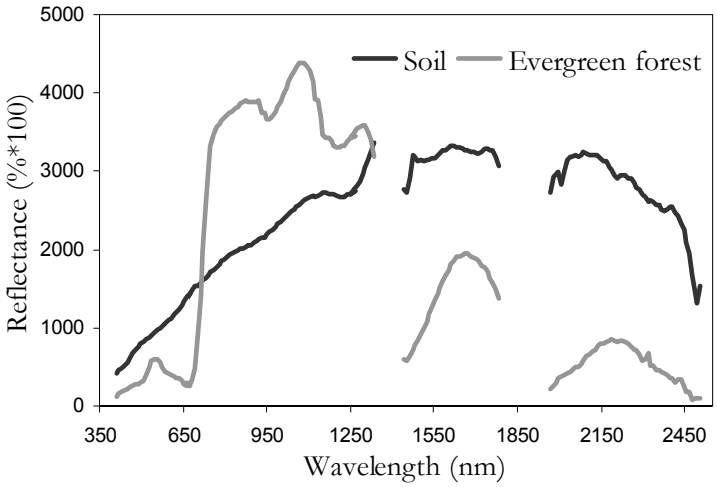

Figure 4. Spectral signatures associated with soil and evergreen forest constituents at AVIRIS Jasper Ridge scene.

(a) Soil (b) Evergreen forest

Figure 5. Fractional abundance maps for soil and evergreen forest in the simulated scene with linear mixtures.

Table 1 shows an experimental study of the sensitivity of unconstrained linear spectral unmixing (LMM) and the proposed HNN/MLP to SNR using the root mean square error (RMSE) as the error metric. Let us denote by N and M the total number of samples and lines in the simulated image. Similarly, let us denote by $\hat{\alpha}_j(x,y)$ the estimated fractional abundance of endmember material $\boldsymbol{r}_j$ in the pixel at spatial coordinates (x,y). Then, we can express the RMSE score associated to fractional abundance estimation of $\boldsymbol{r}_j$ by:

$$\mathrm{RMSE}(\boldsymbol{r}_j)=\left(\frac{1}{N\cdot M}\sum_{x=1}^{N}\sum_{y=1}^{M}\left[\alpha_j(x,y)-\hat{\alpha}_j(x,y)\right]^2\right)^{1/2} \quad (4)$$

Regarding the training of HNN/MLP in this experiment, we used two different training sets. The first training set, designed as training set 1 (TS1), is composed of two AMEE-derived endmembers and 99 additional training samples corresponding to all possible mixtures between $\boldsymbol{r}_1$ and $\boldsymbol{r}_2$. The second training set, designed as training set 2 (TS2), is composed of two AMEE-derived endmembers and 9 additional training samples corresponding to nine representative mixtures between $\boldsymbol{r}_1$ and $\boldsymbol{r}_2$. As illustrated by equation (3), the LMM model is exclusively based on two AMEE-derived endmembers. As shown in Table 1, TS1 and TS2 resulted in very similar results in terms of RMSE in fractional abundance estimation for the considered HNN/MLP.

Table 1. Comparison of RMSE in fractional abundance estimation accuracy for simulated linear mixtures of $\boldsymbol{r}_1$ and $\boldsymbol{r}_2$ by LMM and HNN/MLP using the simulated image in Fig. 5.

Method	Material	No noise	SNR=110:1	SNR=90:1	SNR=70:1	SNR=50:1	SNR=30:1	SNR=10:1
HNN/MLP (TS1)	$\boldsymbol{r}_1$	0	0.0019	0.0020	0.0023	0.0037	0.0061	0.0174
	$\boldsymbol{r}_2$	0	0.0019	0.0019	0.0025	0.0033	0.0060	0.0164
HNN/MLP (TS2)	$\boldsymbol{r}_1$	0	0.0015	0.0018	0.0024	0.0032	0.0054	0.0166
	$\boldsymbol{r}_2$	0	0.0016	0.0019	0.0023	0.0032	0.0055	0.0164
LMM	$\boldsymbol{r}_1$	0	0.0056	0.0065	0.0079	0.0106	0.0192	0.0514
	$\boldsymbol{r}_2$	0	0.0023	0.0032	0.0046	0.0073	0.0158	0.0479

Results in Table 1 reveal that the proposed HNN/MLP neural model seems to be less sensitive than the commonly used LSU in fractional abundance estimation of $\boldsymbol{r}_1$ (soil) and $\boldsymbol{r}_2$ (vegetation). It is also worth noting that HNN/MLP performs considerably better than LSU when the SNR is low, thus revealing that our combined linear/nonlinear approach can outperform the unconstrained LMM method in a noisy environment. Due to the sensitivity of the HNN/MLP to the Alpha parameter, we have developed additional experiments using the simulated image in Fig. 5 in order to determine the influence of Alpha in the number of iterations and CPU time in seconds consumed by the proposed method. Specifically, Table 2 shows the number of iterations and subsequent CPU time for different values of Alpha, where the CPU time in seconds was measured in a specific computing environment based on a Personal Computer with Pentium V Processor at 1.6 GHz and 512 Mb of RAM. It should be noted that scores by HNN/MLP in Table 2 refer to experiments using training set TS2.

Table 2. Number of iterations and CPU time in seconds for different values of Alpha in the HNN/MLP method.

Alpha	10^{-5}	2×10^{-5}	3×10^{-5}	4×10^{-5}	5×10^{-5}	6×10^{-5}	7×10^{-5}	8×10^{-5}	9×10^{-5}	10^{-4}	10^{-3}	10^{-2}	10^{-1}
Iterations	470974	235495	157002	117757	94208	78510	67296	58887	52346	47112	4726	480	44
CPU time	166	108	79	76	76	76	66	64	69	55	62	48	50

As shown in Table 2, when low values are used for the Alpha parameter, both the number of iterations and the CPU time in seconds increase considerably. On other hand, if parameter Alpha is set to an appropriate value, both the number of iterations and processing time can be substantially reduced. Since the setting of the Alpha parameter only affects convergence rate, not the final estimation results, this simple experiment will be used to set the Alpha parameter accordingly in the following experiments, which involve both nonlinear mixture simulations and nonlinear mixtures collected in a real analysis scenario.

4.2. Simulated nonlinear mixtures

This subsection describes our experiments with simulated nonlinear mixtures. We have created a second simulated image with nonlinear mixtures of $\boldsymbol{r}_1$ and $\boldsymbol{r}_2$ using a simple logarithmic function. The 90x90-pixel scene consists of nine vertical regions $R_1,...,R_9$ of ten pixels in width, containing nonlinear mixtures between $\boldsymbol{r}_1$ and $\boldsymbol{r}_2$. The abundances of $\boldsymbol{r}_1$ and $\boldsymbol{r}_2$ were assigned according to equation (5)

$$\boldsymbol{s}(\mathrm{x},\mathrm{y}) = \sum_{\mathrm{j}=1}^{2} \boldsymbol{r}_{\mathrm{j}} \cdot c_{\mathrm{j}}(\mathrm{x},\mathrm{y}) \tag{5}$$

where $c_{\mathrm{j}}(\mathrm{x},\mathrm{y}) = \log \alpha_{\mathrm{j}}(\mathrm{x},\mathrm{y})$ is the contribution of endmember $\boldsymbol{r}_{\mathrm{j}}$ and $\alpha_{\mathrm{j}}(\mathrm{x},\mathrm{y})$ is the fractional abundance of $\boldsymbol{r}_{\mathrm{j}}$. Table 3 shows the fractional abundances assigned to each of the nine simulated regions by means of

equation (5). It should be noted that all the pixels in the simulated scene are mixed in different proportions (there are no pure instances of any material).

Table 3. Abundance assignment for regions in a simulated scene with nonlinear mixtures.

Region	R_1	R_2	R_3	R_4	R_5	R_6	R_7	R_8	R_9
$\alpha_1(x,y)$	0.9	0.8	0.7	0.6	0.5	0.4	0.3	0.2	0.1
$\alpha_2(x,y)$	0.1	0.2	0.3	0.4	0.5	0.6	0.7	0.8	0.9

Table 4 shows an experimental study of the accuracy of linear spectral unmixing (LMM) and the proposed HNN/MLP approach in fractional abundance estimation using the simulated image with nonlinear mixtures described above. Four different training sets were used for the training of the network. The first one, TS1, is composed of nine spectral signatures that represent every possible mixture in the data set. The second one, TS2, uses five out of nine possible mixtures. The third one, TS3, only uses three out of nine possible mixtures. Finally, the fourth considered training set, TS4, uses two AMEE-derived endmembers from the simulated scene. It should be noted that, since there are no pure pixels in the scene, the AMEE algorithm extracted two endmembers that correspond to purest available samples, located in R_1 and R_9 regions, respectively. As reported by Table 4, the lowest RMSE score in abundance estimation was observed when the proposed HNN/MLP method was combined with training set TS1. However, it is also clear from Table 4 that results obtained by HNN/MLP using TS2 and TS3 were very similar in terms of accuracy to those found by HNN/MLP combined by TS1. When HNN/MLP was trained using only the two AMEE-derived endmembers (TS4), the RMSE score was slightly increased. The above result seems to indicate that endmember signatures alone may not be appropriate for training purposes. Although in this case endmember signatures are not completely pure (i.e., they are obtained as the purest available samples) they needed to be combined with additional mixed pixels in order to obtain a representative set of training samples for HNN/MLP. Finally, it is clear from Table 4 that the LMM clearly produced the worst scores in terms of RMSE.

Table 4. Fractional abundance estimation results for simulated nonlinear mixtures of $\boldsymbol{r}_1$ and $\boldsymbol{r}_2$ and resulting RMSE after applying the considered methods.

Material	Abundance	LMM	HNN/MLP (TS1)	HNN/MLP (TS2)	HNN/MLP (TS3)	HNN/MLP (TS4)
$\boldsymbol{r}_1$	0.9	0.975	0.872	0.869	0.873	0.747
	0.8	0.949	0.757	0.757	0.766	0.727
	0.7	0.920	0.673	0.676	0.687	0.705
	0.6	0.887	0.598	0.600	0.616	0.679
	0.5	0.847	0.523	0.530	0.545	0.649
	0.4	0.799	0.440	0.452	0.468	0.612
	0.3	0.737	0.351	0.361	0.378	0.564
	0.2	0.649	0.230	0.242	0.261	0.497
	0.1	0.499	0.038	0.052	0.074	0.382
$\boldsymbol{r}_2$	0.9	0.975	0.867	0.869	0.874	0.747
	0.8	0.949	0.754	0.757	0.766	0.724
	0.7	0.920	0.671	0.676	0.687	0.705
	0.6	0.887	0.597	0.603	0.616	0.679
	0.5	0.847	0.523	0.530	0.545	0.649
	0.4	0.799	0.444	0.452	0.468	0.612
	0.3	0.737	0.353	0.361	0.378	0.564
	0.2	0.649	0.233	0.242	0.261	0.497
	0.1	0.499	0.042	0.053	0.073	0.382
RMSE		0.1101	0.0014	0.0016	0.0021	0.0378

5. Real data experiments

Up to now, computer simulations were used to demonstrate the effectiveness of HNN/MLP in nonlinear spectral mixture analysis. In this section, real spectra collected from nonlinear mixtures will be analyzed. These data, available from Prof. John Mustard's laboratory at Brown University, consisted of 13 data sets collected using the RELAB spectrometer (a high-resolution, bi-directional spectrometer at Brown University). The measurement precision of the RELAB spectrometer is better than 0.25%, which makes it an ideal candidate to evaluate fractional abundance estimation accuracy. The data included spectra from individual endmembers such as Olivine, Enstatite and Magnetite [15], where Fig. 6 plots the three endmember spectra. Most importantly, the data also contained mixtures of these endmembers with abundances listed in Table 5. As a result, the mixture data were the spectra of true mixtures with known abundances for each endmember. In the available Mustard data samples for these mineral types, only nonlinear mixture spectra with associated abundance values were provided [16].

Table 5. Mustard's nonlinear mixture data sets.

Olivine/Enstatite mixtures		Olivine/Magnetite mixtures	
Olivine abundance	Enstatite abundance	Olivine abundance	Magnetite abundance
0.90	0.10	0.95	0.05
0.75	0.25	0.90	0.10
0.50	0.50	0.75	0.25
0.25	0.75	0.50	0.50
0.10	0.90	0.25	0.75

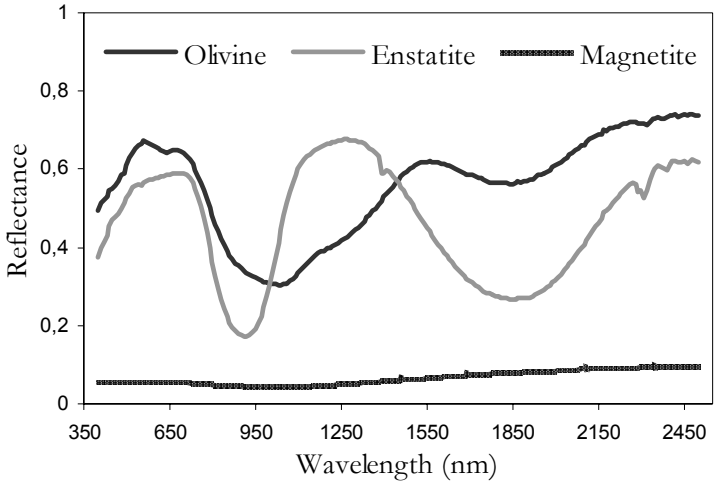

Figure 6. Mustard's endmember spectra.

Tables 6 and 7 show an experimental study of the accuracy of linear spectral unmixing (LMM), Guilfoyle and Chang's previously developed nonlinear abundance estimation method which uses RBF neural networks, and the proposed HNN/MLP approach in the task of estimating fractional abundances using Mustard's data. Mixtures of Olivine/Enstatite and Olivine/Magnetite are respectively considered. While the training for RBF was accomplished as specified in the literature, three different training sets were used for the proposed HNN/MLP. The first training set (TS1) is composed of a representative spectrum of all possible mixtures. The second training set (TS2), is composed of three out of five possible mixtures. Finally, the third training set (TS3) contains no mixture data at all, only spectra corresponding to pure mineral signatures. For illustrative purposes, results obtained using the simple LMM as well as results obtained by using Guilfoyle and Chang's approach [8] based on RBF neural networks are also reported.

From experimental results in Tables 6 and 7, we can conclude that the proposed HNN/MLP model can accurately estimate the abundance of endmember materials in nonlinear mixtures, provided that the training set contains a representative set of mixed signatures. When nonlinear mixtures of Olivine and Enstatite were considered (see Table 6), we found that the HNN/MLP model trained only with spectral endmembers (TS3) cannot perform better than the simple LMM. However, when training sets made up of mixed signatures (TS1 and TS2) were used, the proposed HNN/MLP clearly outperformed both the LMM and Guilfoyle and Chang's RBF-based method. It is important to note that no significant difference was sought in the abundance estimation accuracy when TS1 or TS2 were used, a fact that reveals that a judicious selection of mixed spectra can help reduce the number of required training samples.

Table 6. Fractional abundance estimation results for real nonlinear mixtures of Olivine and Enstatite and resulting RMSE after applying the considered methods.

Material	Abundance	LMM	RBF	HNN/MLP (TS1)	HNN/MLP (TS2)	HNN/MLP (TS3)
Olivine	0.90	0.880	0.881	0.916	0.913	0.879
	0.75	0.704	0.700	0.736	0.730	0.703
	0.50	0.452	0.443	0.479	0.468	0.452
	0.25	0.244	0.210	0.266	0.251	0.244
	0.10	0.115	0.121	0.115	0.117	0.115
Enstatite	0.90	0.886	0.835	0.886	0.890	0.886
	0.75	0.727	0.761	0.731	0.721	0.725
	0.50	0.535	0.551	0.521	0.517	0.534
	0.25	0.298	0.295	0.263	0.267	0.298
	0.10	0.133	0.114	0.083	0.091	0.133
RMSE		0.0010	0.0012	0.0003	0.0003	0.0010

On other hand, when nonlinear mixtures of Olivine and Magnetite were considered, it is clear from Table 7 that Guilfoyle and Chang's RBF-based method performed the best, with the proposed HNN/MLP producing very close results in terms of abundance estimation when both TS1 and TS2 were used as training sets. Using only endmember signatures for training produced better results than those found by the standard LMM, but the overall accuracy in terms of RMSE decreased as compared to that found by RBF and HNN/MLP with other considered training sets.

Table 7. Fractional abundance estimation results for real nonlinear mixtures of Olivine and Magnetite and resulting RMSE after applying the considered methods.

Material	Abundance	LMM	RBF	HNN/MLP (TS1)	HNN/MLP (TS2)	HNN/MLP (TS3)
Olivine	0.95	0.843	0.946	1.000	0.965	1.000
	0.90	0.697	0.899	0.883	0.831	0.879
	0.75	0.457	0.765	0.651	0.599	0.608
	0.50	0.255	0.576	0.533	0.435	0.329
	0.25	0.102	0.300	0.411	0.298	0.138
Magnetite	0.75	0.895	0.693	0.643	0.708	0.995
	0.50	0.741	0.407	0.513	0.559	0.789
	0.25	0.533	0.199	0.184	0.187	0.271
	0.10	0.298	0.075	0.136	0.127	0.191
	0.05	0.153	0.031	0.053	0.030	0.059
RMSE		0.0429	0.0024	0.0057	0.0044	0.0285

Overall, experiments in Tables 6 and 7 demonstrate that nonlinear abundance estimation methods generated a substantially better mass fraction estimate than did the LMM in Mustard's data. These results, combined with those found in computer simulations, indicate that the proposed HNN/MLP method worked well on both linearly and nonlinearly mixed data, in particular, when an appropriate set of training samples was selected for the learning stage [17].

6. Conclusions and future research

This paper has described a combined HNN/MLP neural network for estimating the abundance of endmember materials in hyperspectral images. The proposed neural model integrates the concepts of linear and nonlinear unmixing. In a first stage, a rough estimation of concentrations is accomplished by HNN via LMM. This initial estimation is refined by MLP in a second step using nonlinear mixing concepts. The experiments conducted in this paper have shown that the proposed HNN/MLP model is a useful tool for performing abundance estimation in both simulated and real hyperspectral imagery data, in particular, when the data are dominated by nonlinear mixing effects. Since the HNN/MLP used in this analysis is a hybrid of linear and nonlinear estimators, it can be easily adapted to either the linear or nonlinear mixture model. An important issue for successful application of the combined HNN/MLP model is the selection of an appropriate set of training samples for supervised learning. In this work, we have explored different training sets composed by several combinations of endmember signatures as well as mixed signatures. From our experiments, we conclude that endmember signatures alone cannot define an appropriate training set for the network, which also requires other types of training samples such as mixed signatures for successful exploitation. Future work will investigate four different types of signatures: pure (endmember), mixed, anomalous and homogeneous to develop appropriate mechanisms to generate a set of good training samples for HNN/MLP in unsupervised mixed pixel classification [17]. Also, since the experiments presented in this paper only consisted of binary mixtures which were intended to show the usefulness of the proposed method, further experiments with ternary or quaternary mixtures are highly desirable.

Acknowledgements

The authors would like to acknowledge Dr. Robert O. Green and the AVIRIS team at NASA's Jet Propulsion Laboratory for their advice and support to this work. Javier Plaza would also like to express his gratitude to Prof. Chein-I Chang at University of Maryland, Baltimore County, for his suggestions during a research visit to his Remote Sensing Signal and Image Processing Laboratory (RSSIPL). Antonio Plaza would like to thank the Spanish Ministry of Education and Science for its support (PR2003-0360 Fellowship).

References

[1] N. Keshava and J.F. Mustard, "Spectral unmixing," *IEEE Signal Processing Magazine*, vol. 19, pp. 44-57, 2002.

[2] C.-I Chang, *Hyperspectral imaging: spectral detection and classification*, Kluwer Academic/Plenum Publishers, New York, 2003.

[3] G.A. Carpenter, S. Gopal, S. Macomber, S. Martens and C.E. Woodcock, "A neural network method for mixture estimation for vegetation mapping," *Remote Sensing of Environment*, vol. 70, pp. 138-152, 1999.

[4] J. Plaza, P. Martínez, R. Pérez, A. Plaza, M.C. Cantero, "Nonlinear neural network-based mixture model for estimating the concentration of nitrogen salts in turbid inland waters using hyperspectral imagery," *SPIE Optics East Conference, Chemical and Biological Standoff Detection*, Philadelphia, Pennsylvania, USA, 2004.

[5] M.C. Cantero, R. Pérez, P. Martínez, P.L. Aguilar, J. Plaza and A. Plaza, "Analysis of the behaviour of a neural network model in the identification and quantification of hyperspectral signatures applied to the determination of water quality," *SPIE Optics East Conference, Chemical and Biological Standoff Detection*, Philadelphia, Pennsylvania, USA, 2004.

[6] R. Pérez, P. Martínez, A. Plaza and P.L. Aguilar, "Systolic array methodology for a neural model to solve the mixture problem," in *Neural Networks and Systolic Array Design*, World Scientific: Singapore, 2002.

[7] C.M. Bishop, *Neural networks for pattern recognition*, Oxford University Press: Oxford, 1995.

[8] K.J. Guilfoyle, M.L. Althouse and C.-I Chang, "A quantitative and comparative analysis of linear and nonlinear spectral mixture models using radial basis neural networks," *IEEE Transactions on Geoscience and Remote Sensing*, vol. 39, no. 8, Aug. 2001.

[9] A. Plaza, P. Martínez, R. Pérez and J. Plaza, "Spatial/spectral endmember extraction by multidimensional morphological operations," *IEEE Transactions on Geoscience and Remote Sensing*, vol. 40, pp. 2025-2041, 2002.

[10] A. Plaza, P. Martínez, R. Pérez and J. Plaza, "A quantitative and comparative analysis of endmember extraction algorithms from hyperspectral data," *IEEE Transactions on Geoscience and Remote Sensing*, vol. 42, no. 3, pp. 650-663, March 2004.

[11] J. Plaza, A. Plaza, P. Martínez and R. Perez, "Nonlinear mixture models for analyzing laboratory simulated-forest hyperspectral data," *SPIE Image and Signal Processing for Remote Sensing*, Barcelona, Spain, 2003.

[12] J. Plaza, A. Plaza, P. Martínez, R. Pérez, "H-COMP: A tool for quantitative and comparative analysis of endmember identification algorithms," *IEEE International Geoscience and Remote Sensing Symposium*, Toulouse, France, 2003.

[13] R.O. Green et al., "Imaging spectroscopy and the airborne visible/infrared imaging spectrometer (AVIRIS)," *Remote Sensing of Environment*, vol. 65, pp. 227–248, 1998.

[14] J. C. Harsanyi and C.-I Chang, "Hyperspectral image classification and dimensionality reduction: An orthogonal subspace projection approach," *IEEE Transactions on Geoscience and Remote Sensing*, vol. 32, pp. 779–785, 1994.

[15] K.J. Guilfoyle and C.-I Chang, "Application of linear and nonlinear mixture models for hyperspectral imagery analysis using radial basis function neural networks," *Ph. D. Dissertation*, University of Maryland, Baltimore County, 2001.

[16] J.F. Mustard and J.M. Sunshine, "Spectral analysis for earth science investigation," in *Remote Sensing for the Earth Sciences*, Wiley: New York, 1999.

[17] J. Plaza, C.-I Chang, P. Martínez, R. Pérez and A. Plaza, "On the generation of training samples for neural network-based mixed pixel classification," submitted to *SPIE Defense and Security Symposium*, Orlando, Florida, USA, 2005.